ACS APPLIED NANO MATERIALS



www.acsanm.org
Article

# Electrochemical Design of Gold Nanostructures for Controllable Electrochemical Performance and Scalable Aptamer Sensing Application

Feixiong Chen,* Bahar Mostafiz, Johanna Suni, and Emilia Peltola*

Cite This: https://doi.org/10.1021/acsanm.5c00962



**ABSTRACT:** A simple electrochemical method for designing gold nanostructures was developed by programming deposition potentials, enabling surface nanoengineering of screen-printed electrodes. As a result of this method, we have observed three distinct growth modes of gold nanostructures, which, depending on their various morphologies, are Needle-shaped gold nanostructures (one dimensionally dominated mode), leaf-shaped gold nanostructures (two-dimensionally dominated mode), and coral-shaped gold nanostructures (three-dimensionally dominated mode). All gold nanostructures exhibited an enhanced electrochemical response to the redox solution, improved reversibility, and reduced impedance, compared to the unmodified electrodes, albeit to varying degrees. We demonstrated the superior antifouling performance of the coral-shaped gold nanostructures in a redox solution containing bovine serum albumin, compared to other gold nanostructures. Finally, to assess another aspect of differences in the electrochemical sensing behaviors, we constructed an aptamer sensor for progesterone detection, where the needle-shaped gold nanostructures showed the highest signal gain using Electrochemical Impedance Spectroscopy, in comparison to that of leaf-shaped and coral-shaped gold nanostructures. We envision that the proposed method will potentially enable the design or fabrication of desirable gold nanostructures with increasingly complex or hierarchical structures, bearing promising applications in wide sensing and biomedical applications.

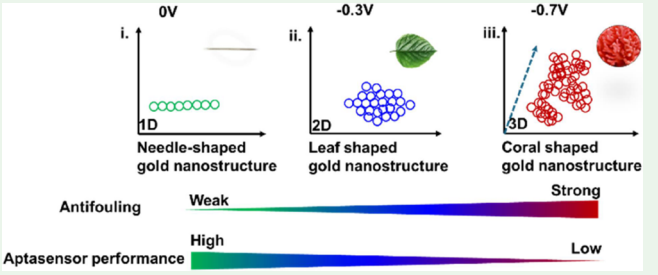


**KEYWORDS:** *gold nanostructures, electrochemical deposition, electrochemical sensing, biofouling, aptamer immobilization*



## 1. INTRODUCTION

Screen-printed electrodes (SPEs) have been widely used in biosensors,[1,2] drug analysis,[3] and diagnostic assays.[4,5] Owing to their portability, cost-effectiveness, and ease of electroanalysis, SPEs are recognized as a promising approach for advanced point-of-care diagnostics for rapid detection,[6−8] as they can provide sensitive results with easy-to-handle equipment in short turnaround times. However, due to limitations in the screen-printing process, SPEs have a few setbacks. Commercially available SPEs often have a reduced electroactive surface area (ESA) due to the inherent limitations of the screen-printing process. Additionally, the presence of substrate layers made of synthetic polymeric materials can introduce insulating effects, hindering electron transfer and affecting the electrode's overall performance. These issues directly affect the adsorption properties and reproducibility of SPEs in broad applications.[9] Currently, it is still challenging to improve the electrode's electroanalytic performance via surface engineering, which is a vital criterion in electrochemical analysis.

There is a growing interest in developing electrochemical deposition methods as a cost-effective solution to address these shortcomings. Indeed, electrochemical deposition enables the formation of a variety of gold nanostructures (GNSs) at the electrode surface, such as the flower-like gold microstructure,[10] gold hierarchical microstructures,[11−13] gold nanoplates,[14] dendritic GNS,[15,16] and gold nanoparticles.[17−19] The diverse morphologies of GNS can affect the electrode's sensitivity[20,21] and specificity,[22,23] allowing researchers to use them in a wide range of applications, such as well-known electrochemical biosensors.[17] Indeed, Kumar et al.[25] reported the fabrication of nanoporous gold modified electrodes at high voltage, where such a significantly high ESA was obtained, resulting in improved sensitivity. Additionally, Ritz et al.[24] also investigated the control of gold morphology to enhance aptamer modification and sensor performance. However, most researchers have primarily focused on increasing the surface area by depositing different GNS to enhance electron transfer between biomolecules and electrodes.

Received: February 17, 2025
Revised: April 25, 2025
Accepted: April 29, 2025





https://doi.org/10.1021/acsanm.5c00962
ACS Appl. Nano Mater. XXXX, XXX, XXX−XXX

**Scheme 1. Schematic Illustration of the Fabrication of Varying Gold Nanostructures upon the SPE Surface**[a]

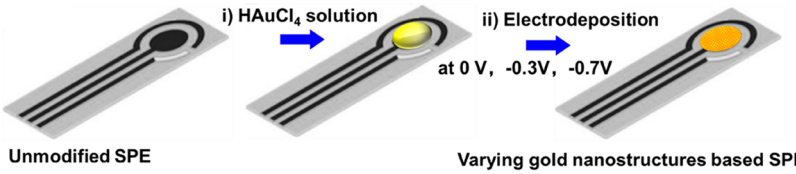


[a](i) Loading the $HAuCl_4$ solution at the working electrode surface and (ii) controlling the electrodeposition voltage at 0, −0.3, and −0.7 V to design the gold nanostructures upon the working electrode of SPE.

Currently, there is still limited understanding about how the GNS affects electrochemistry and sensor performance. To address this issue, a systematic study of the impact of different GNS on electrochemistry, biofouling, and sensor performance is needed to bridge the gap between nanomaterials to their performance. This approach could allow us to design optimal GNS that improve conductivity, electron transfer, sensitivity, and stability of the electrodes. Ultimately, a comprehensive understanding of GNS in electrochemistry will provide a strong foundation for effective SPE customization.

In this work, we propose a design strategy for electrochemical deposition to fabricate a well-defined GNS on SPEs, as illustrated in Scheme 1. This strategy enables controlled electrochemical sensing performance and provides a scalable approach for surface nanoengineering. By controlling the applied potential and deposition time within an electrochemical system,[25,26] various GNS—including needle-shaped GNS (N-GNS), leaf-shaped GNS (L-GNS), and coral-shaped GNS (C-GNS)—were electrochemically fabricated. This allows for a comprehensive understanding of designable GNS at the SPE surface by studying the impact of their morphology on the sensing performance and electrochemical properties. The electrochemical design strategy proposed here offers a valuable approach for nanotechnology and nanomaterials, with potential applications in healthcare technology.[27−30]

## 2. EXPERIMENTAL SECTION

**2.1. Chemicals and Apparatus.** Bovine serum albumin (BSA), 6-mercapto-1-hexanol (MCH), tris(2-carboxyethyl) phosphine hydrochloride (TCEP), magnesium chloride ($MgCl_2$), hexaammineruthenium(III) chloride ($[Ru(NH_3)_6]Cl_3$), potassium hexacyanoferrate(II) trihydrate ($K_4Fe(CN)_6{\cdot}3H_2O$), potassium ferricyanide ($K_3Fe(CN)_6$), gold(III) chloride trihydrate ($HAuCl_4{\cdot}3H_2O$), sulfuric acid 98% ($H_2SO_4$), sodium chloride (NaCl), and disodium phosphate ($Na_2HPO_4$) were all purchased from Sigma-Aldrich. Potassium chloride (KCl) and potassium dihydrogen phosphate ($KH_2PO_4$) were purchased from VWR. Deionized (DI) water was produced by Milli-Q, Millipore, with a resistivity of 18.2 MΩ·cm. All chemicals were used as received.

Gold screen printed electrodes (SPE, ItalSens IS-W1-2.C1.RS.50) were purchased from Palmsens (Netherlands) as the working electrodes (WE). Two reference electrodes (RE) were used. The first one, labeled as RE-1, was an Ag/AgCl reference electrode with a porous Teflon tip (CHI111) from CH Instruments, Inc. (USA), which was used inside the sulfuric solution. And RE-2 was an Ag/AgCl refillable reference electrode with a diameter of 6.0 mm, and the length of 70 mm was from redox.me (Sweden), which was specific for their use in the PBS electrolyte. Platinum (Pt) wire (diameter 0.5 mm, 99.99%) used as the counter electrode was from Sigma-Aldrich.

A phosphate buffer saline (PBS) solution was prepared by dissolving 80 g of NaCl, 2.0 g of KCl, 14.4 g of $Na_2HPO_4$, and 2.4 g of $KH_2PO_4$ in 10.0 L of deionized water with a final pH of 7.4. The stock sulfuric acid (98%) was diluted to different concentrations (50.0 mM, 0.5 M, and 1.0 M of $H_2SO_4$) by adding the DI water. 10.0 mM of $HAuCl_4$ solution was prepared by dissolving 473.0 mg of $HAuCl_4{\cdot}3H_2O$ in 120.0 mL of 1.0 M $H_2SO_4$.

The electrochemical deposition was performed with a Palmsens EmStat4 potentiostat. Aside from SPE's internal microelectrode working electrode, other electrodes were connected externally. Although the SPE had working electrode, counter electrode, and reference electrode components, its reference electrode was destroyed in the 1.0 M $H_2SO_4$. To avoid the interference of the reference electrode performance, we chose to use the conventional one in our study, ensuring that our deposition process and testing are controlled. Thus, a Pt wire was used as the counter electrode and an Ag/AgCl electrode (RE-1) as the reference electrode, while the working electrode performance of SPE was the key for our observation in this work. All potentials mentioned in this publication are quoted with respect to the Ag/AgCl reference potential.

**2.2. Electrochemical Deposition of Gold Nanostructures for the Surface Nanoengineering of SPE.** All SPEs were subjected to electrochemical polishing. After they were immersed in 50.0 mL of 0.5 M $H_2SO4$, cyclic voltammetry (CV) was performed for 3 cycles, in the potential range of 0−1.4 V with the scan rate of 0.1 $V{\cdot}s^{-1}$. After the polishing step was done, the SPEs were rinsed and then immersed in 40.0 mL of 10.0 mM $HAuCl_4$ solution. The gold deposition was carried out using chronoamperometry. Throughout the experiments, the deposition potential was set either on 0, −0.3, or −0.7 V. Deposition times of 60, 120, 240, and 400 s were initially tested. After deposition, a chronoamperometric step at −1.2 V was applied for 10 s to reduce gold oxides.

**2.3. Physical Characterization of GNS-Based SPEs.** Scanning electron microscopy (SEM) was conducted via a Thermo Scientific FE-SEM Apreo S instrument for surface imaging of SPEs. X-ray photoelectron spectroscopy (XPS) analysis was performed with a ThermoFisher ESCAlab 250 imaging X-ray photoelectron spectrometer (Al K$\alpha$ (1486.68 eV), 500 $\mu$m spot size, 50 eV pass energy, 0.1 eV step size). The crystallographic orientation of the deposited layers was assessed by X-ray diffraction (XRD) performed in an empyrean XRD instrument from Malvern Panalytical, equipped with a Cu K$\alpha$ source ($\lambda$ = 1.5418 Å), in the 2$\theta$ window from 30° to 120°, with a scan step of 0.05°. Attension theta optical tensiometer (Biolin Scientific, Japan) was used for contact angle measurement conducted with the DI water droplets (5.0 $\mu$L).

**2.4. Calculation of the Electrochemical Surface Area.** The electroactive surface areas (ESA) of SPEs were calculated using the gold oxide reduction peak current obtained in 50 mM $H_2SO_4$, where the potential ranged from 0 to 1.4 V, with a scan rate of 0.1 $V{\cdot}s^{-1}$. ESA was determined by integrating the current peak, with a charge density of 386 $\mu C{\cdot}cm^{-2}$,[31] which corresponds to a full monolayer of gold oxide ($N$ = 3).

**2.5. Characterization of Electrochemical Measurement and Biofouling Behavior.** CV and square wave voltammetry (SWV) were utilized to study the electrochemical performance of SPEs in 3.0 mM $[Ru(NH_3)_6]^{3+}$ and 3.0 mM $[Fe(CN)_6]^{4-}$. Both scan rates for SWV and CV were 100 $mV{\cdot}s^{-1}$ in the potential range from −0.6 to 0.2 mV for $[Ru(NH_3)_6]^{3+}$ and from −0.4 to 0.8 V for $[Fe(CN)_6]^{4-}$.

For biofouling experiments by using outer sphere redox (OSR), SPEs were immersed in the biofouling solution prepared with 40.0 mg $mL^{-1}$ of BSA in 3.0 mM $[Ru(NH_3)_6]^{3+}$. Electrochemical measurement of CV and SWV was tested under different incubation times, such as 0, 0.5, 16, and 40 h. The protein concentration in plasma/


https://doi.org/10.1021/acsanm.5c00962
ACS Appl. Nano Mater. XXXX, XXX, XXX−XXX

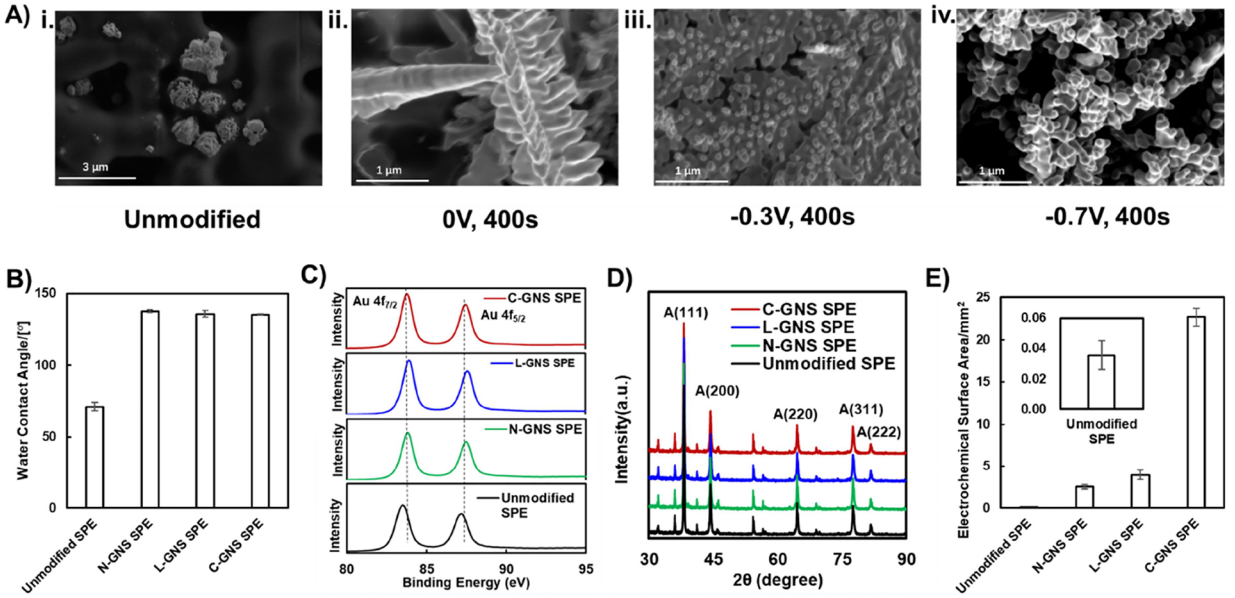


**Figure 1.** (A) SEM image of gold nanostructured SPE (unmodified, i) surfaces prepared at applied potentials of 0 V (ii), −0.3 V (iii), −0.7 V (iv) for 400 s. (B) Water contact angle degree on different GNS-based SPE. (C) X-ray photoelectron spectroscopy (XPS) spectra showing the Au 4f band of different GNS-based SPE. (D) X-ray diffraction (XRD) pattern of GNS-based SPE. (E) Estimation of the electrochemical surface area (ESA) of different GNS based SPE by CV running in 50.0 mM $H_2SO_4$.

serum is approximately 60−80 mg·mL$^{-1}$, of which about 50−60% are albumins, corresponding to used 40 mg·mL$^{-1}$ concentration.

For biofouling experiments by using inner sphere redox (ISR), the SPEs were immersed in the biofouling solution prepared with 2.0 mg·mL$^{-1}$ of BSA in 3.0 mM $[Fe(CN)_6]^{4-}$), so as to measure their CV and SWV at the incubation time of 0, 0.5, 15, and 40 h. To mitigate biofouling effects, diluted samples are frequently employed. Consequently, we employed 2.0 mg mL$^{-1}$ concentration for $[Fe(CN)_6]^{4-}$.

Each sample was scanned by CV and SWV for 3 cycles and three times ($N$ = 3), where CV displayed the biofouling performance, and the peak current of SWV was used to quantify the signal reduction ratio for these SPEs before and after biofouling.

**2.6. Fabrication of the Aptamer Sensors.** All modified aptamers used in this study were purchased from Metabion (Germany). Aptamer sequences were chosen for Progesterone (P4) and modified with a six-carbon thiol linker on the 5′ ends and a redox marker of methylene blue (MB), on the 3′end. The P4-specific aptamer sequence with an MB-label was 5′-SH-(CH2)6-GCA TCA CAC ACC GAT ACT CAC CCG CCT GAT TAA CAT TAG CCC ACC GCC CAC CCC CGC TGC -MB-3′, the dissociation constant ($K_d$) values of which were 17 nM.[32,33]

The aptamer solutions were prepared in PBS(a) solution (10 mM of $NaH_2PO_4$, $K_2HPO_4$, 1.0 M NaCl and 2.0 mM $MgCl_2$, pH = 6.6−7.2). Additionally, PBS(a) was used as the electrolyte for electrochemical analysis with or without P4 analyte binding. Before immobilizing the aptamer onto the SPE surface, 9.0 μL of 10.0 mM TCEP (the reducing agent) was added to reduce the disulfide bonds in 3.0 μL of 100 μM aptamer solution and left in the dark for 1 h to incubate. This activated aptamer solution was then diluted with a PBS(a) solution to a 1.0 μM concentration.

A 20.0 μL amount of activated aptamer was drop-casted on the working electrode surface of SPE for a 16 h incubation (overnight) under wet conditions (4 °C) inside a plastic dish. To passivate the surface and remove any nonspecifically adsorbed aptamer, the SPEs were placed in 10.0 mM MCH for 2h. After being rinsed with DI water, all SPEs were immersed in DI water before electrochemical measurements.

**2.7. Measurements and Analysis of the Aptamer Sensor.** CV is an electrochemical method that is often used for electrochemical characterization. To this end, CV experiments for the fabricated aptamer sensor were performed in the potential range of −0.4 to −0.1 V with a scan rate of 100 mV·s$^{-1}$. SWV is utilized as a reliable method to record the CV is an electrochemical method often used for electrochemical characterization. To this end, CV experiments for the fabricated aptamer sensor were performed in the potential range of −0.4 V to −0.1 V with a scan rate of 100 mV·s$^{-1}$. SWV is utilized as a reliable method to record the redox peaks because it eliminates the background current to a significant degree. The current was measured in a potential range of −0.4 to −0.1 V with an SWV amplitude of 50 mV and a frequency of 100 Hz.

**2.8. Sensing Performance Characterization by P4 binding.** A stock solution of P4 (27.0 mM) was prepared in ethanol. It was further diluted to a P4 4.0 μM solution in PBS(a). 40.0 μL of P4 4.0 μM was drop-casted on an SPE surface and left for a 1.0 h incubation at room temperature. After removing the supernatant, the SPE was immersed in $[Fe(CN)_6]^{3-}/[Fe(CN)_6]^{4-}$ 3.0 mM in PBS(a) for electrochemical impedance spectroscopy (EIS) analysis. The EIS of each SPE was measured before and after P4 binding. where the $E_{dc}$ were 0.2404 V for unmodified SPE, 0.2001 V for N-GNS SPE, 0.1951 V for L-GNS SPE, and 0.2051 V for C-GNS(120s) SPE.

Additionally, to establish the SPE relationship between scan rates and peak current intensity, different scan rates from 0.05 to 0.6 V·s$^{-1}$ were tested via CV.

## 3. RESULTS AND DISCUSSION

**3.1. Surface Characterization of GNS-SPEs.** We investigated how variations in GNS-SPE morphology influenced the electrochemical performance, biofouling, aptamer immobilization, and impedance of aptasensors. As a first step, different types of electrochemically synthesized GNS were classified. The redox potential-driven reaction of chloroauric acid ($HAuCl_4$) initiates at the innermost surface of the SPE, leading to the formation of gold crystals. As the deposition time increases, these crystals further grow toward the outermost surface of the nanostructures.[34−36]

Previous research suggests that the electric field influences the ion distribution, which in turn affects growth behavior.[25,27] Here, we applied different deposition potentials (0, −0.3, and −0.7 V) and deposition times (10, 60, 120, 180, 400 s) to grow


https://doi.org/10.1021/acsanm.5c00962
ACS Appl. Nano Mater. XXXX, XXX, XXX−XXX

the desired GNS at the SPE surface and to control the electrochemical deposition process. Considering that the gold deposits did not exhibit single-crystal characteristics, it was not practical to describe the individual size of each gold nanostructure (GNS). Therefore, we focused on characterizing the GNS collectively to evaluate their overall effects in this study. To examine the impact of electrochemical deposition conditions on the GNS structure, we characterized the surface morphology of prepared GNS-SPE by SEM Figure 1A-i shows the unmodified SPE.[37−39] Our results demonstrate that this method enables the controlled fabrication of GNS by adjusting the deposition potential. Specifically: (1) a deposition potential at 0 V vs Ag/AgCl resulted in the needle-shaped GNS (N-GNS), (2) a deposition potential at −0.3 V vs Ag/AgCl resulted in a leaf-shaped GNS (L-GNS), and (3) a deposition potential to −0.7 V vs Ag/AgCl resulted in coral-shaped GNS (C-GNS), as shown in Figure 1A (ii-iv). A broader range of SEM magnifications is presented in Figure S1A−C.

Higher negative potentials corresponded to an increased current density during the deposition process (Table S1). We assumed that the lower current density observed at 0 V vs Ag/AgCl slowed the gold deposition process, leading to predominantly one-dimensional (1D) growth mode, as illustrated in Figure S1D-i. At −0.3 V vs Ag/AgCl, the GNS growth behavior transitioned from 1D to two-dimensional (2D) growth (Figure S1D-ii). Since the gold deposition process is dependent on the current density, the process accelerated significantly at −0.7 V. Due to the ultrahigh current density at this potential, gold growth behavior became highly random and was dominated by a 3D growth mode, as shown in Figure S1D-iii. Significantly, the electrochemical design strategy proposed here provides a convenient and simple method for controlling the growth modes of GNS, enabling the successful fabrication of three distinct GNS morphologies, i.e., as N-GNS, L-GNS, and C-GNS. Importantly, the deposition time did not appear to influence the GNS shape, as demonstrated in Figure S2.

The water contact angles (WCA, $\theta$) of the prepared GNS-SPE surfaces were measured to investigate the wettability properties, as shown in Figures 1B and S3. The unmodified SPE had a relatively hydrophilic interface ($\theta = 71 \pm 3°$), while all GNS-SPEs had a highly hydrophobic surface. The WCAs of N-GNS, L-GNS, and C-GNS were measured to be $\theta = (138 \pm 1)°$, $\theta = (136 \pm 2)°$, and $\theta = (135.1 \pm 0.4)°$, respectively. We further compared the WCA of C-GNS(400 s) to C-GNS(120 s) with $\theta = (137 \pm 1)°$, to confirm that there was no noticeable difference in WCA between GNS. These results indicate that surface nanoengineering transformed the SPEs from hydrophilic to hydrophobic. The deposition of GNS was responsible for this change.[40,41]

XPS measurements were conducted on GNS-SPE surfaces to analyze the chemical state of the gold atoms. Figure 1C displays the XPS pattern of a high-resolution narrow scan for Au 4f for the unmodified SPE, which was deconvoluted into two spin−orbit splitting components. The XPS peaks at 83.5 and 87.1 eV correspond to the binding energies of Au 4f7/2 and Au 4f5/2, respectively.[16,42] Both peaks exhibited slight negative shifts compared to the standard values of bulk Au metal.[43,44] However, this observation strongly supports the identification of deposited GNS as zerovalent gold.[45] As shown in Figure 1C, the binding energies of the GNS-SPEs were further observed at 83.8 eV for Au 4f7/2 and 87.5 eV for Au 4f5/2 (see Table S2). Compared with unmodified SPE, electrochemical deposition of GNS reduced the negative shifts in the gold XPS binding energies.

The gold atomic content was estimated by using XPS. The unmodified SPE had a low gold atomic content of 2.3%. However, gold deposition significantly increases this to 19.5% for N-GNS, 28.6% for L-GNS, and 45.0% for C-GNS (Table S2). As expected, a higher deposition current resulted in a greater gold atomic content. Furthermore, the gold atomic content of C-GNS(120 s) was further determined to be 32.5%, indicating that the deposition time influenced the gold atomic content during the deposition process. These results suggest that the GNS shape is primarily controlled by the electrochemical deposition potential, while deposition time controls the amount of gold deposited on the SPE surface.

The crystalline structure of electrochemically deposited Au in N-GNS, L-GNS, and C-GNS was analyzed by using XRD. Figure 1D shows five characteristic diffraction peaks at 38.1°, 44.4°, 64.5°, 77.7°, and 81.6°, corresponding to the (111), (200), (220), (311), and (222) planes of face-centered cubic Au.[46] These findings confirm that the growth behavior of GNS electrodeposits is dependent on the externally applied potential, while the intrinsic crystal structure remains unaffected during electrochemical deposition.

**3.2. Electrochemical Properties of GNSs.** Higher negative potentials were associated with increased current density involved in the deposition process (Table S1). As a part of preliminary testing, the GNS-based SPEs prepared with different deposition times were characterized by their electrochemical response versus a solution of 1.0 mM $[Ru(NH_3)_6]^{3+}$. For comparison, the SWV peak intensities of unmodified SPE and GNS-SPEs with different deposition times are shown in Figure S4.

The lower the deposition potential, the longer the deposition time required to reach the maximum peak intensity. For example, (i) at a deposition potential of 0 V vs Ag/AgCl, the maximum SWV peak current was observed at 400 s, (ii) at −0.3 V vs Ag/AgCl, the maximum SWV peak current was reached at 180 s and did not show further improvement up to 400 s of deposition time, (iii) at −0.7 V vs Ag/AgCl, the maximum SWV peak current occurred around 120 s but decreased with longer deposition times. Therefore, we selected C-GNS(120 s) prepared at 120s under −0.7 V as the reference for comparisons with N-GNS and L-GNS.

The prepared GNS exists in 1D, 2D, and 3D configurations, resulting in different coverages of the SPE surface and particle distribution. This variation can be characterized by quantifying the ESA of the deposited SPEs through the gold oxidation/reduction cycles in CV scans.[26,31] Based on the CV data presented in Figure S5A, the ESAs of GNS were determined (as shown in Figure 1E). The unmodified SPEs exhibited a geometrical area of 3.14 $mm^2$, corresponding to their design size. However, its ESA was estimated to be around $0.035 \pm 0.010$ $mm^2$, with a narrow distribution. This discrepancy is due to the partial passivation of the SPE surface caused by the deposition of gold nanoparticles during the screen-printing fabrication process (Figure 1A). In contrast, as shown in Figure 1E, the ESA values for N-GNS, L-GNS, and C-GNS were determined to be approximately $2.5 \pm 0.3$, $3.9 \pm 0.6$, and $23 \pm 1$ $mm^2$, respectively. These results show that the ESA of the GNS on the SPE was significantly improved in the following order: C-GNS> L-GNS > N-GNS.

The ESA of C-GNS was further quantified under more deposition times (60, 120, 240, and 400 s, see Figure S5B). C-


https://doi.org/10.1021/acsanm.5c00962
ACS Appl. Nano Mater. XXXX, XXX, XXX−XXX

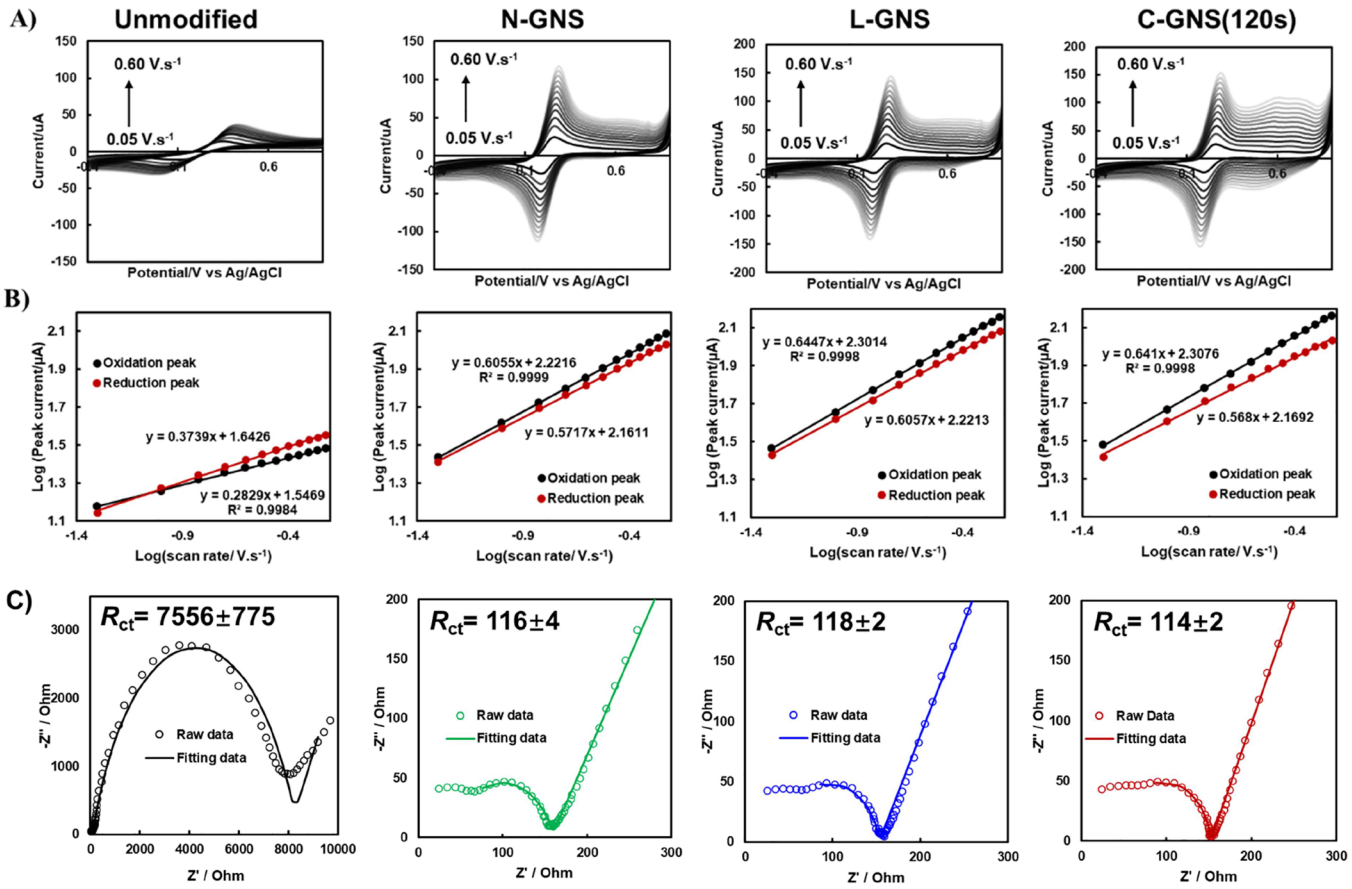


**Figure 2.** (A) Cyclic voltammograms of 3.0 mM $[Fe(CN)_6]^{3-}/[Fe(CN)_6]^{4-}$ with different scan rates from 0.05 to 0.60 V·s$^{-1}$. (B) Linear relationship between the logarithm of peak current and the logarithm of scan rate. (C) Nyquist plot of EIS for different GNS-based SPEs.

**Table 1. Oxidation Potential ($E_{pa}$/mV), Peak Separation ($\Delta E_p$/mV), Oxidation Current ($I_{pa}/\mu$A), Ratio of Oxidation and Reduction Current ($I_{pa}/I_{pc}$), Heterogeneous Electron-Transfer Rate Constant ($k^0$/cm·s$^{-1}$), and Pseudocapacitance ($C_{dl}/\mu$F·mm$^{-2}$) of Different SPEs for 3.0 mM of $[Fe(CN)_6]^{3-}/[Fe(CN)_6]^{4-}$ in PBS ($N > 3$)[a]**

| samples | $E_{pa}$/mV | $\Delta E_p$/mV | $I_{pa}/\mu$A | $I_{pa}/I_{pc}$ | $k^0$/cm·s$^{-1}$ | $C_{dl}/\mu$F·mm$^{-2}$ |
|---|---|---|---|---|---|---|
| unmodified SPE | 363 ± 13 | 340 ± 16 | 18 ± 1 | 1.0 ± 0.1 | (0.242 ± 0.005) × 10$^{-3}$ | 58 ± 2 |
| N-GNS(400 s) | 262 ± 1 | 77 ± 3 | 42 ± 1 | 1.1 ± 0.0 | (0.349 ± 0.004) × 10$^{-3}$ | 131 ± 2 |
| L-GNS(400 s) | 265 ± 5 | 81 ± 13 | 43 ± 1 | 1.1 ± 0.0 | (0.347 ± 0.006) × 10$^{-3}$ | 132 ± 5 |
| C-GNS(400 s) | 261 ± 3 | 62 ± 3 | 69 ± 2 | 1.4 ± 0.0 | (0.394 ± 0.004) × 10$^{-3}$ | 190 ± 5 |
| C-GNS(120 s) | 261 ± 3 | 65 ± 5 | 46 ± 1 | 1.2 ± 0.0 | (0.361 ± 0.005) × 10$^{-3}$ | 137 ± 2 |

[a]All the SPE with the working electrode area of 3.14 mm$^2$.

GNS(120 s) exhibited an ESA of 7.73 ± 0.4 mm$^2$, which was close to that of N-GNS(400 s) and L-GNS(400 s). Meanwhile, C-GNS(120s) showed a similar intensity in the SWV response to 1.0 mM $[Ru(NH_3)_6]^{3+}$ as that of N-GNS(400 s) and L-GNS(400 s). We further analyzed the peak currents ($I_{pa}$) obtained from SWV for various GNS-SPEs as a function of each electrode's ESA. This relationship was mapped in Figure S6A and Figure S6B, using both the OSR and ISR probes to assess how electron transfer behavior correlates with the ESA of each GNS-SPE. N-GNS, L-GNS, and C-GNS(120s) show similar behavior in this regard.

To investigate the main role of nanostructured features of GNS on antifouling, electrochemical properties, and electrochemical sensing performance, and to minimize the influence of ESA in the electrochemical performance evaluation, we primarily selected the C-GNS(120 s) prepared at 120 s under −0.7 V as a comparison for N-GNS and L-GNS.

### 3.3. Electrochemical Behavior of GNS-SPEs.

The surface geometric structures of GNS-SPEs primarily influence their electrochemical behavior. To evaluate their electrochemical performance, we first measured the electron transfer kinetics by using a diffusible redox mediator through CV at various scan rates, as shown in Figure 2A.

Electrode can exhibit a reversible redox reaction with fast one-electron transfer kinetics for the equimolar electroactive couple ($[Fe(CN)_6]^{3-}/[Fe(CN)_6]^{4-}$). The oxidation−reduction CV peak parameters (shown in Table 1) indicated significant improvements for the modified SPEs. For the various GNS-SPEs (N-GNS, L-GNS, and C-GNS(120 s)), the $\Delta E_p$ values were all below 80 mV, demonstrating fast electron transfer. In contrast, the $\Delta E_p$ of the unmodified SPE was measured to be 340 ± 16 mV (greater than 100 mV), suggesting a sluggish electron transfer.


https://doi.org/10.1021/acsanm.5c00962
ACS Appl. Nano Mater. XXXX, XXX, XXX−XXX

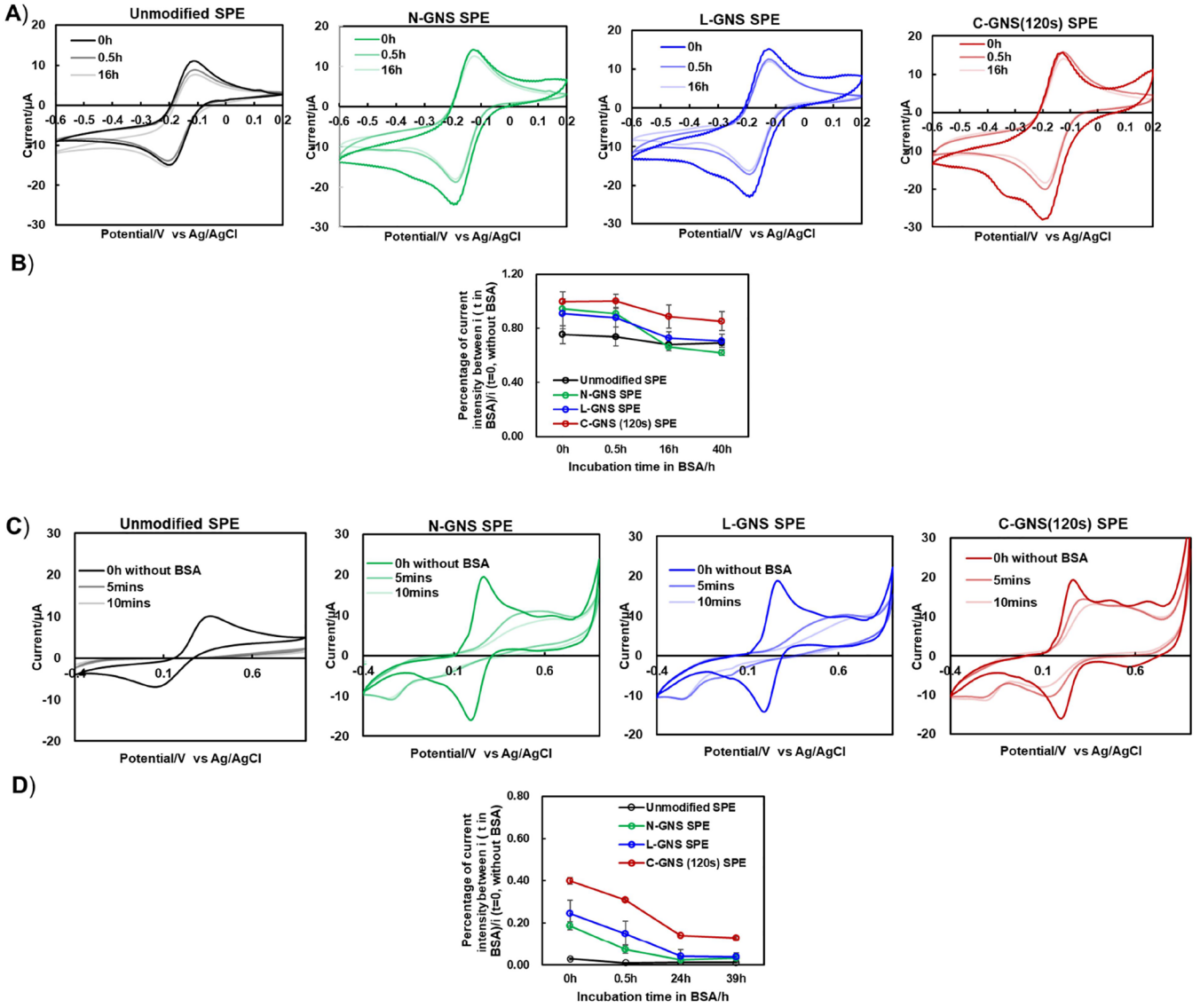


**Figure 3.** Electrochemical characterization and biofouling performance of different GNS based SPEs. (A) CV of nanostructured SPE measured in 3.0 mM $[Ru(NH_3)_6]^{3+}$ without and with 40.0 mg·mL$^{-1}$ BSA, at 0 h (without BSA), 0.5 h (with BSA) and 16 h (with BSA), (B) their SWV peak current intensity reduction of 3.0 mM $[Ru(NH_3)_6]^{3+}$ caused by biofouling in 40.0 mg·mL$^{-1}$ of BSA solution at 0, 0.5, 16, and 40 h. (C) CV of nanostructured SPE measured in 3.0 mM $[Fe(CN)_6]^{4-}$ without and with 2.0 mg·mL$^{-1}$ BSA, at 0 h (without BSA), 5 min (with BSA), and 10 min (with BSA), and (D) their SWV peak current intensity reduction of in 3.0 mM $[Fe(CN)_6]^{4-}$ caused by biofouling in 2.0 mg·mL$^{-1}$ BSA solution at 0, 0.5, 16, and 40 h.

Additionally, we calculated the heterogeneous electron-transfer rate constant ($k^0$, cm·s$^{-1}$) based on the scan rates to evaluate the electrochemical reaction kinetics.[47] Table 1 presents the average $k^0$ values for all SPEs, clearly demonstrating that the electrodeposition of GNS improves electrochemical kinetics. The GNS-SPEs exhibited slightly $k^0$ higher values ($0.349 \times 10^{-3}$–$0.394 \times 10^{-3}$ cm·s$^{-1}$) compared to the unmodified SPE ($k^0 = 0.242 \times 10^{-3}$ cm·s$^{-1}$). Notably, the different morphologies of GNS-SPEs showed similar $k^0$ values.

The oxidation/reduction ratio ($I_{pa}/I_{pc}$) (see Figure 2A) serves as a qualitative indicator of redox reaction characteristics, assessing reversibility. The unmodified SPE had an $I_{pa}/I_{pc}$ ratio of 1.0 ± 0.1, indicating a reversible reaction, while the $I_{pa}/I_{pc}$ ratios of GNS-SPEs ranged from 1.1 to 1.4, indicating quasi-reversible reactions.

In electrochemistry, the scan rate is a key factor in distinguishing diffusion-controlled electrochemistry from thin-layer electrochemistry with confined mass transfer.[48] To determine whether the process was controlled by diffusion or adsorption, we analyzed the relationship between the logarithm of peak current (log $I_p$) and the logarithm of scan rate (log $\nu$) for all SPEs (Figures 2B, S7, and Table S3). A slope of ≤0.5 indicates a diffusion-controlled process, while a slope of ≥1.0 suggests an adsorption-controlled reaction.[49]

The observed slope value for all GNS-SPEs was close to 0.5, confirming that the redox reaction on their surfaces was predominantly diffusion-controlled.[47] Based on the Randles–Ševčík equation,[50] the slopes of log $I_{pc}$ vs log $\nu$ (log $I_{pa}$ vs log $\nu$) were measured as follows: 0.58 ± 0.01 (0.61 ± 0.01) for N-GNS, 0.62 ± 0.02 (0.67 ± 0.03) for L-GNS and 0.58 ± 0.01 (0.56 ± 0.02) for C-GNS(120s). The slope deviation from 0.5 suggests the presence of thin-film effects, slow kinetics, or a


https://doi.org/10.1021/acsanm.5c00962
ACS Appl. Nano Mater. XXXX, XXX, XXX−XXX

combination of diffusion and surface interactions among GNS-SPEs. However, the differences between the various GNS-SPEs were minor.

In contrast, the unmodified SPE exhibited a slope of 0.36 ± 0.01 (0.28 ± 0.01), which is significantly lower than 0.5, likely due to slow kinetics.

Moreover, the pseudocapacitance ($C_{dl}$) of the electrical double layer for each SPE was calculated from the CVs recorded in the same redox system,[51,52] as shown in Table 1. The $C_{dl}$ of for the unmodified SPE was 58 ± 2 $\mu$F·mm$^{-2}$, whereas it was measured as 131 ± 2 $\mu$F·mm$^{-2}$ for N-GNS, 132 ± 2 $\mu$F·mm$^{-2}$ for L-GNS, 190 ± 5 $\mu$F·mm$^{-2}$ for C-GNS(400 s), and 137 ± 2 $\mu$F·mm$^{-2}$ for C-GNS(120 s).

EIS is a powerful technique for characterizing the electron transfer and mass transfer properties of an electrode.[53] The Nyquist plot of EIS for the prepared GNS-SPEs is shown in Figure 2C. The semicircles in the plots, which indicate electron transfer kinetics,[48,54] decrease in size following electrode modification compared to the unmodified SPE, demonstrating improved electrochemical reactivity of the designed GNS-SPEs.

The equivalent circuit was used to fit the impedance plot for parameter calculations, with the charge transfer resistance ($R_{ct}$) measured as follows: 7555 ± 775 Ω·cm$^2$ for the unmodified one, 116 ± 4 Ω·cm$^2$ for N-GNS, 118 ± 2 Ω·cm$^2$ for L-GNS, 114 ± 2 Ω·cm$^2$ for C-GNS(120 s), and 112 ± 3 Ω·cm$^2$ for C-GNS(400 s) (Figures 2C and S7). Significantly, these varying GNS-based SPE presented 65-fold lower than the unmodified one with regard to the charge transfer resistance. All GNS-SPEs showed similar EIS behavior in the same redox system, further indicating their similar ESA of gold deposition

Overall, the GNS-SPEs enhanced the electron transfer kinetics compared with the unmodified SPE, with only minor differences among them.

**3.4. Biofouling Performance of Varying GNS-Based SPEs Using the OSR Probe.** Since both biofouling and the immobilization of the biorecognition element rely on adsorption, we aimed to compare these processes to understand their similarities and differences on various GNS. We used BSA as a representative model foulant protein.[55] When adsorbed on the SPE surface, proteins hinder electron transfer at the electrode interface. This disruption is observed in CV experiments, where fouling is indicated by two main changes: an increase in peak separation ($\Delta E_p$) and a decrease in peak current ($I_p$) for an electroactive molecule in solution.

To evaluate the antifouling performance of our GNS-SPEs, we investigated their electron transfer behavior in the presence and absence of BSA at various time points. In this section, we first used an ionic OSR probe ($[Ru(NH_3)_6]^{3+}$) to evaluate biofouling effects. Since OSR reactions occur without specific interactions with the electrode, they serve as a reliable indicator of the electrode's electronic properties, with or without BSA-induced fouling.[56]

$[Ru(NH_3)_6]^{3+}$ demonstrated nearly ideal electron transfer kinetics on these different GNS-SPEs as well as the unmodified SPE (Figure 3A), where the CVs obtained at pH 7 have a typical diffusion-controlled peak shape for a reversible redox probe. Table S4 summarizes the electron transfer kinetics of the measured probes. The $\Delta E_p$ values serve as indicators of the electron transfer kinetics with shifts potentially associated with protein adsorption.

Before biofouling, the $\Delta E_p$ values of $[Ru(NH_3)_6]^{3+}$ were measured as 82 ± 3 mV for unmodified SPE, 59 ± 3 mV for N-GNS, 62 ± 3 mV for L-GNS, and 45 ± 5 mV for C-GNS(120 s), as shown in Table S4. These results indicate that the GNS-deposited SPEs exhibit lower $\Delta E_p$, suggesting slightly faster electron transfer kinetics compared with the unmodified one. Notably, the C-GNS(120 s) electrode presented more ideal electron transfer kinetics for $[Ru(NH_3)_6]^{3+}$ compared with that of N-GNS and L-GNS.

After 0.5 h of biofouling in 40.0 mg·mL$^{-1}$ BSA, the $\Delta E_p$ values of $[Ru(NH_3)_6]^{3+}$ were increased slightly to 89 ± 3 mV (unmodified SPE), 64 ± 3 mV (N-GNS), 65 ± 0 mV (L-GNS) and 65 ± 0 mV (C-GNS(120 s)), as detailed in Table S4. Importantly, for the OSR probes, there were no statistically significant changes in the $\Delta E_p$ values after 0.5 and 16 h of biofouling.

To quantify the biofouling resistance of these prepared GNS-SPEs, we measured the time-dependent changes in the redox intensity of 3.0 mM $[Ru(NH_3)_6]^{3+}$ during the BSA fouling, where the redox intensity percentage ratio was calculated by using the redox signal intensity of SWV measured with and without any BSA.

In the initial biofouling period of 0−0.5 h from Figure 3B, the current intensities affected by the biofouling effect were calculated to be approximately 0.75−0.74 mV for the unmodified one, 0.94−0.91 mV for N-GNS 0.91−0.88 mV for L-GNS and 1.0−1.0 mV for C-GNS(120 s) compared to original current prior to fouling. In short periods of protein exposure, fouling has little effect on $[Ru(NH_3)_6]^{3+}$ detection on the GNS-SPE surfaces.

With prolonged BSA exposure (16−40 h), the current intensity decreased to 0.68−0.69 for the unmodified SPE, 0.66−0.62 for N-GNS SPE, 0.73−0.71 for L-GNS SPE, and 0.88−0.85 for C-GNS(120 s) SPE. Among the tested electrodes, C-GNS(120 s) exhibited the best antifouling performance compared to L-GNS and N-GNS.

Additionally, the biofouling performance of C-GNS(400 s) was evaluated (Figure S8A) in comparison to C-GNS(120 s). The redox intensity percentage increased from 1.03 to 1.9 after 40 h of biofouling. This suggests that the OSR probe may have penetrated the complexed C-GNS surface, likely due to its characteristic surface structure and high ESA.

**3.5. Biofouling Performance of Varying GNS-Based SPEs Using the ISR Probe.** Compared with the OSR, the ISR probe interacts more strongly with the electrode surface. This may provide insight into BSA biofouling on different electrode surfaces and its effects on electrochemical performance.[57] Here, we also measured the responses of an ISR probe ($[Fe(CN)_6]^{4-}$) in the presence of BSA.

The initial CV responses of ($[Fe(CN)_6]^{4-}$) were similar in prepared GNS-SPEs but different from those of the unmodified one (Figure 3C).

As we deposited different gold nanostructures on the SPEs, there may form different surface microenvironments for redox interaction on the electrode. The varying interaction of the redox species with the electrode surface can lead to multiple peaks.[58] From Figure S8B, we observed pronounced, strong multiple peaks in CV, which were more prominent than in other samples compared to others. This can be attributed to the overdeposited, coral-shaped gold nanostructure that creates a complex microenvironment, contributing to the emergence of distinct multiple peaks. $\Delta E_p$ of $[Fe(CN)_6]^{4-}$ was observed to be 309 ± 10 mV for the unmodified SPE, while for GNS-SPEs it was 57 ± 3, 65 ± 5, and 65 ± 0 mV for N-GNS, L-GNS, and C-GNS(120 s), respectively (see Table S4). This


https://doi.org/10.1021/acsanm.5c00962
ACS Appl. Nano Mater. XXXX, XXX, XXX−XXX

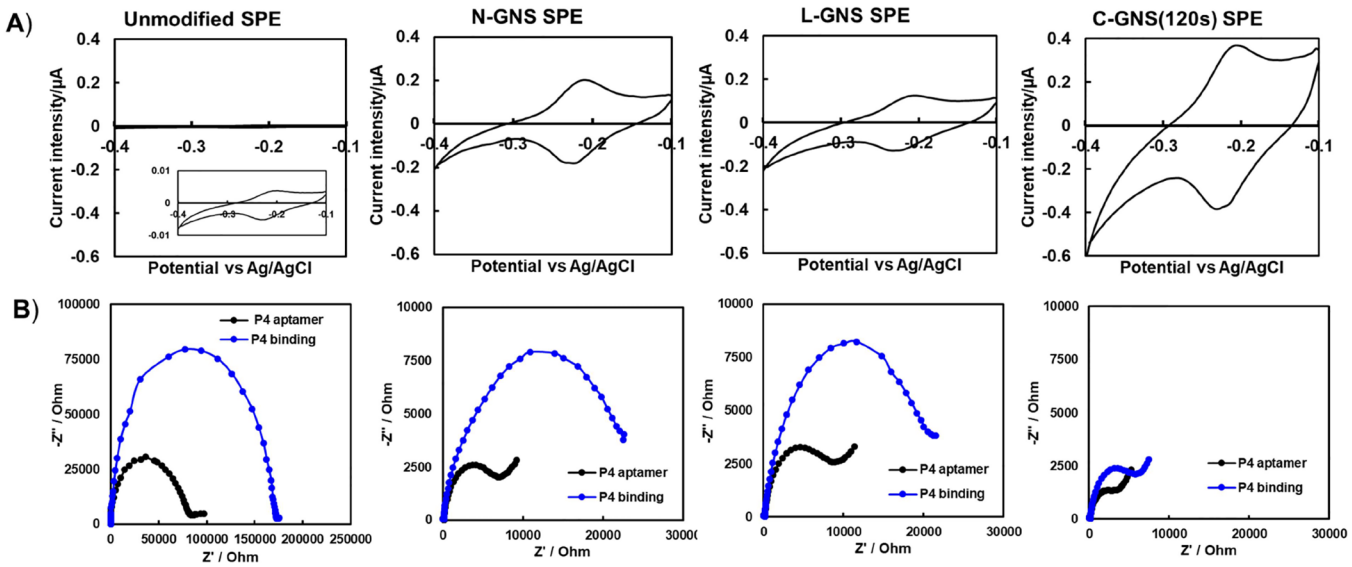


**Figure 4.** Electrochemical characterization of nanostructured SPE after MB-aptamer immobilization in 10 mM PBS (2.0 mM of $MgCl_2$) (A) CV of nanostructured SPE after aptamer immobilization, (B) EIS of nanostructured SPE with P4 aptamer immobilization and after P4 binding (2.0 $\mu$M of P4 solution prepared in 10.0 mM PBS (2.0 mM of $MgCl_2$, 1.0 M NaCl) after 30 min binding incubation.

demonstrated the improved reversibility of $[Fe(CN)_6]^{4-}$ on the GNS-SPEs. Similar to Section 3.4, the electrochemical signals of GNS SPEs were measured in 3.0 mM $[Fe(CN)_6]^{4-}$ with or without 2.0 mg·mL$^{-1}$ BSA in a set time frame.

Figure 3C shows the impact of BSA exposure (0, 5, and 10 min) on the CV response for $[Fe(CN)_6]^{4-}$. The very different responses observed across various SPEs indicated that GNS morphologies were playing a critical role in electrochemical interactions. Specifically, the unmodified SPE showed the weakest antifouling performance since the CV response was undetectable within 5 min, and the electrochemical signal disappeared. $\Delta E_p$ significantly increased in all GNS-SPEs, especially after 10 min of BSA exposure. N-GNS SPE and L-GNS SPE $\Delta E_p$ values increased to 856 ± 41 mV (increased by 1401%) and 918 ± 36 mV (increased by 1312%), respectively. Interestingly, the C-GNS(120 s) SPE with a lower $\Delta E_p$ of 174 ± 4 mV (increased by 168%) presented a better antifouling performance. Compared to that of C-GNS(120 s), C-GNS(400 s) with a long gold deposition time exhibited a narrower $\Delta E_p$ of 124 ± 14 mV (increased by 175%), demonstrating an excellent antifouling under the presence of BSA (Figure S8B).

As displayed in Figure 3D, we further assessed the antifouling performance of each SPE under similar exposure times (0, 0.5, 24, and 39 h). During biofouling at 0 and 0.5 h, BSA significantly reduced peak current intensity. Specifically, the peak current intensity reduced to 3−1% of the original nonfouled signal for unmodified SPE, to 19−7% for N-GNS, to 25−15% for L-GNS, and to 40−31% for C-GNS. After biofouling for 24 and 39 h, the redox peak current percentage of each SPE was stabilized to be 1% for unmodified, 2% for N-GNS, 4% for L-GNS, and 14% for C-GNS(120 s). This demonstrates that the C-GNS SPE surface exhibits superior antifouling performance compared to other tested samples. Notably, the C-GNS(400 s) exhibited a redox peak current of 30% after prolonged biofouling, as shown in Figure S8B.

Although C-GNS deposited SPE can support the penetration of redox probe from the SPEs' surface to their inside, owing to the complexed coral structure, the relatively large size of BSA may be retained at the C-GNS surface, hindering access to the internal surface of C-GNS for biofouling.[52] We demonstrated that the developed geometrical structures enabled faster reaction kinetics and a lower current drop when using the OSR and ISR probes under BSA fouling conditions. The three-dimensional C-GNS structure provided the most robust response preservation for both the OSR and ISR probes under the fouling process.

**3.6. Characterization of Aptamer Immobilization at GNS-SPEs.** Given that these GNS-SPES modifications are more than mere surface roughening, we first evaluated the conjugation of the aptamer onto the SPEs to assess the impact of GNS on the electrochemical sensing performance of the fabricated electrochemical-aptamer-based biosensors (E-AB). Due to their diverse morphologies, GNS can influence the immobilization efficiency of the aptamer on the SPE surface, thereby affecting the overall electrochemical sensing performance.

For the fabrication of E-AB, we initially selected the P4 aptamer, labeled with a terminal redox probe (MB).[32] The primary role of MB was to assess the aptamer conjugation on the SPE surface. By calculating the charge transfer density, we estimated the amount of the MB bound to the electrode surface, which is equivalent to the amount of aptamer.[24]

The redox signal of MB, in both CV and SWV scanning, indicated successful aptamer conjugation, as shown in Figures 4A and S9.

To determine the amount of aptamer conjugation on each SPE, we calculated the integration of the area under the CV reduction peak. The outcome was the charge reduction of the MB-aptamer when it was immobilized on the SPE surface. As depicted in Figure S9A, the conjugation amount of immobilized aptamer on each SPE was measured to be 0.0091 ± 0.00 pmol for the unmodified one, 0.46 ± 0.04 pmol for N-GNS, 0.26 ± 0.03 pmol for L-GNS, and 0.37 ± 0.09 pmol for C-GNS (120 s).

To investigate the correlation between ESA and aptamer conjugation, we further examined C-GNS (400 s), which had the highest amount of conjugation, up to 0.65 ± 0.09 pmol.


https://doi.org/10.1021/acsanm.5c00962
ACS Appl. Nano Mater. XXXX, XXX, XXX−XXX

This was attributed to the ultrahigh ESA for C-GNS (400 s). Consequently, we primarily compared the N-GNS, L-GNS, and C-GNS (120 s) in Figure S9B, as all exhibited comparable ESA. Among them, the N-GNS SPE, with the lowest ESA, provided the highest aptamer conjugation amount. C-GNS (120 s) showed higher aptamer immobilization than L-GNS, likely due to its slightly higher ESA. This confirmed that the GNS structures affect aptamer immobilization efficiency beyond their impact on surface area.

Moreover, the calculated aptamer packing density, obtained by dividing the aptamer amount on each electrode ESA, exhibited a decreasing trend: N-GNS > L-GNS > C-GNS(120 s) as depicted in Figure S9C. While gold electrodeposits contributed to higher ESA on SPEs and increased binding surface area for aptamer conjugation, the aptamer packing density on varying GNS-based SPE surfaces did not improve. The unmodified SPE with the lowest ESA presented the highest aptamer packing density. Meanwhile, C-GNS(400 s), with ultrahigh ESA and aptamer conjugation amount, showed the lowest aptamer packing density. This demonstrated a strong relationship between aptamer packing density and ESA; further investigation is needed to optimize their electrochemical sensing performance.

Additionally, the $\Delta E_p$ of the MB-labeled aptamer was less than 25 mV among all the aptamer-immobilized SPEs. This indicated that the surface property of SPE had minimal impact on the electrochemical properties of MB estimated from Figure 4A.[59]

**3.7. Electrochemical Sensing Performance by EIS of P4 Binding Testing.** To minimize the impact of ESA on sensing performance, we primarily compared the E-AB with SPE surfaces designed by N-GNS, L-GNS, and C-GNS(120 s) to investigate the critical parameters of GNS for sensor performance. EIS, a powerful technique for analyzing interfacial properties associated with biorecognition events on electrode surfaces, was used as a key electroanalytical method. This method offered high sensitivity and potential for label-free detection. Herein, we adopted impedance methods to explore the differences in their electrochemical sensing performance.[53,60−62] A single P4 concentration must be sufficient to induce the aptamer sensing performance, in pursuit of the maximum signal gain for our sensor investigation.

Figure 4B displays the Nyquist plots of EIS spectra of varying GNS-based SPEs with only P4 aptamer, recorded under 3.0 mM of $[Fe(CN)_6]^{3-}/[Fe(CN)_6]^{4-}$ in PBS(a) buffer (pH = 7.4). Compared with the bare GNS-SPEs (Figure 2C), the resistance of aptamer immobilization significantly increased. To analyze their electrochemical sensing performance, we recorded the Nyquist plots for each SPE where the aptamer completely captured the P4 targets after a 30 min incubation with P4 solution. The EIS spectra of P4 binding showed an increased resistance compared to that of only the P4 aptamer, demonstrating a clear electrochemical sensing response using the EIS method. To quantify the signal gain caused by P4 binding, we calculated the resistance of $R_{ct}$ for each SPE before and after P4 binding using the Zview software. As shown in Figure S10, the calculated signal gain from EIS was estimated to be 464 ± 333% for N-GNS, 307 ± 18% for L-GNS, and 246 ± 146% for C-GNS(120 s), compared to 111 ± 54% for the unmodified one. This demonstrated that the N-GNS enhanced the sensitivity of P4 measurement; the resulting improvements were attributed to higher aptamer immobilization, packing density, and signal strength compared to other GNS-based SPEs.

## 4. CONCLUSIONS

We introduced a simple chronoamperometric methodology to electrochemically design varying GNS at SPEs. We utilized different deposition potentials to obtain morphologies of N-GNS, L-GNS, and C-GNS. Based on their similar performance in XRD, WCA, and XPS, we demonstrated that the applied deposition potential significantly influenced the growth behavior of these GNS. Specifically, N-GNS exhibited a 1D-dominated growth mode, L-GNS a 2D growth mode, and C-GNS a 3D growth mode. Additionally, the GNS-SPEs exhibited a high surface area of ESA compared to the unmodified SPE. In terms of their electrochemical properties, the GNS-based SPEs presented faster electron transfer kinetics and improved reversibility, leading to amplified electrochemical signals compared to the unmodified SPE. The resistance of varying GNS was reduced in impedance spectra, but showed no significant difference among them.

We investigated the antifouling capacity of varying GNS and found that the C-GNS demonstrated excellent antifouling properties, specifically due to their coral structure design with increased heterogeneity in gold electrodeposits, effectively preventing biofouling.

We built a sensor platform by functionalizing these GNS surfaces with a specific bioprobe aptamer. This allowed us to assess the aptamer immobilization efficiency and biosensing performance. We found that varying GNS affected the aptamer immobilization efficiency, with N-GNS exhibiting the highest aptamer conjugation amount and packing density compared to those of L-GNS and C-GNS(120 s). Impedance sensing revealed no difference between the GNSs.

In summary, our electrochemical design strategy is a relatively straightforward and rapid method to engineer the surface of SPEs with a designable GNS, improving sensitivity and sensing performance. Because each GNS, with its distinct growth mode, can function independently or collaboratively, we have the potential for creating complex three-dimensional (3D) hierarchical microarchitectures at the SPE, which could further enhance sensing performance. Meanwhile, the varying GNS-based SPE also opens the door for utilization in other types of sensors that leverage the functionalization of the SPE surface for point-of-care use, providing highly sensitive detection of DNA, protein, and small molecule binding events.

## ■ ASSOCIATED CONTENT

### Data Availability Statement

The data are available from the corresponding author upon reasonable request.

### Supporting Information

The Supporting Information is available free of charge at https://pubs.acs.org/doi/10.1021/acsanm.5c00962.

Calculation equations of electrochemical data; deposition parameters for all SPEs; XPS of all SPEs; calculated slopes of log $I_p$ vs log $v$ for all SPEs; $\Delta E_p$ of all SPEs for biofouling; SEM images for all SPEs; C-GNS morphologies under deposition time; contact angle images of all SPEs; All SPEs tested under 1.0 mM of $[Ru(NH_3)_6]^{3+}$; ESA of all SPEs; relationship map of ESA and redox species; electrochemistry of C-GNS(400 s); biofouling of C-GNS(400 s); aptamer conjugation calculations for


https://doi.org/10.1021/acsanm.5c00962
ACS Appl. Nano Mater. XXXX, XXX, XXX−XXX

all SPEs; and impedance sensor signal gain for all SPEs (PDF)

## AUTHOR INFORMATION


### Corresponding Authors

**Feixiong Chen** − *Disease Networks Research Unit, Faculty of Biochemistry and Molecular Medicine, University of Oulu, 90014 Oulu, Finland; Department of Mechanical and Materials Engineering, University of Turku, 20014 Turku, Finland;* orcid.org/0000-0001-9053-1128; Email: feixiog.chen@oulu.fi

**Emilia Peltola** − *Department of Mechanical and Materials Engineering, University of Turku, 20014 Turku, Finland;* orcid.org/0000-0002-8868-9273; Email: emilia.peltola@utu.fi

### Authors

**Bahar Mostafiz** − *Department of Mechanical and Materials Engineering, University of Turku, 20014 Turku, Finland*

**Johanna Suni** − *Department of Mechanical and Materials Engineering, University of Turku, 20014 Turku, Finland;* orcid.org/0000-0002-6694-3576

Complete contact information is available at: https://pubs.acs.org/10.1021/acsanm.5c00962


### Author Contributions

F.C. contributed to the study conception and design, material preparation, experiments, data collection, and analysis. The first draft of the manuscript was written by F.C. B.M. contributed to SEM experiments, draft writing, reviewing, and editing. J.S. contributed to experiments. E.P. provided supervision, financial support and draft reviewing and editing. All authors read and approved the final manuscript.


### Funding

We acknowledge funding from The Research Council of Finland under the Scientific Council for Natural Sciences and Engineering with project No. 352891 and 355747. F.C. acknowledges the Proof-of-Concept (PoC) funding 2025 from the University of Oulu and the City of Oulu with project No. 24305099116. The work was conducted under the #SUSMAT umbrella.


### Notes

There is no ethical issue in this study.

The authors declare no competing financial interest.

## ACKNOWLEDGMENTS


FC acknowledges the great support from Dr. Ilari Angervo (Wihuri Physical Laboratory, Department of Physics and Astronomy, University of Turku, Finland) for XRD testing of our samples, from Dr. Sari Granroth (Department of Physics and Astronomy, University of Turku, 20014, Turku, Finland) for XPS measurement of our samples. The authors are thankful to the Materials Research Infrastructure (MARI) at the University of Turku for infrastructural facilities.


## REFERENCES


(1) Stanković, D. M.; Milanović, Z.; Švorc, Ľ.; Stanković, V.; Janković, D.; Mirković, M.; Đurić, S. V. Screen Printed Diamond Electrode as Efficient "Point-of-Care" Platform for Submicromolar Determination of Cytostatic Drug in Biological Fluids and Pharmaceutical Product. *Diam. Relat. Mater.* **2021**, *113*, No. 108277.

(2) Taleat, Z.; Khoshroo, A.; Mazloum-Ardakani, M. Screen-Printed Electrodes for Biosensing: A Review (2008−2013). *Microchim. Acta* **2014**, *181*, 865−891.

(3) Kelíšková, P.; Matvieiev, O.; Janíková, L.; Šelešovská, R. Recent Advances in the Use of Screen-Printed Electrodes in Drug Analysis: A Review. *Curr. Opin. Electrochem.* **2023**, *42*, No. 101408.

(4) Mincu, N. B.; Lazar, V.; Stan, D.; Mihailescu, C. M.; Iosub, R.; Mateescu, A. L. Screen-Printed Electrodes (SPE) for in Vitro Diagnostic Purpose. *Diagnostics* **2020**, *10* (8), 517.

(5) Li, M.; Li, Y. T.; Li, D. W.; Long, Y. T. Recent Developments and Applications of Screen-Printed Electrodes in Environmental Assays-A Review. *Anal. Chim. Acta* **2012**, *734*, 31−44.

(6) Calucho, E.; Álvarez-Diduk, R.; Piper, A.; Rossetti, M.; Nevanen, T. K.; Merkoçi, A. Reduced Graphene Oxide Electrodes Meet Lateral Flow Assays: A Promising Path to Advanced Point-of-Care Diagnostics. *Biosens. Bioelectron.* **2024**, *258*, No. 116315.

(7) García-Miranda Ferrari, A.; Rowley-Neale, S. J.; Banks, C. E. Screen-Printed Electrodes: Transitioning the Laboratory in-to-the Field. *Talanta Open* **2021**, *3*, No. 100032.

(8) Ahmadi, A.; Khoshfetrat, S. M.; Kabiri, S.; Dorraji, P. S.; Larijani, B.; Omidfar, K. Electrochemiluminescence Paper-Based Screen-Printed Electrode for HbA1c Detection Using Two-Dimensional Zirconium Metal-Organic Framework/Fe3O4 Nanosheet Composites Decorated with Au Nanoclusters. *Microchim. Acta* **2021**, *188*, 296.

(9) Suresh, R. R.; Lakshmanakumar, M.; Arockia Jayalatha, J. B. B.; Rajan, K. S.; Sethuraman, S.; Krishnan, U. M.; Rayappan, J. B. B. Fabrication of Screen-Printed Electrodes: Opportunities and Challenges. *J. Mater. Sci.* **2021**, *56* (15), 8951−9006.

(10) Guo, S.; Wang, L.; Wang, E. Templateless, Surfactantless, Simple Electrochemical Route to Rapid Synthesis of Diameter-Controlled 3D Flowerlike Gold Microstructure with "Clean" Surface. *Chem. Commun.* **2007**, 3 (30), 3163−3165.

(11) Soleymani, L.; Fang, Z.; Lam, B.; Bin, X.; Vasilyeva, E.; Ross, A. J.; Sargent, E. H.; Kelley, S. O. Hierarchical Nanotextured Microelectrodes Overcome the Molecular Transport Barrier to Achieve Rapid. *Direct Bacterial Detection. ACS Nano* **2011**, *5* (4), 3360−3366.

(12) Zhu, C.; Meng, G.; Huang, Q.; Huang, Z.; Chu, Z. Au Hierarchical Micro/Nanotower Arrays and Their Improved SERS Effect by Ag Nanoparticle Decoration. *Cryst. Growth Des.* **2011**, *11* (3), 748−752.

(13) Sadat Mousavi, P.; Smith, S. J.; Chen, J. B.; Karlikow, M.; Tinafar, A.; Robinson, C.; Liu, W.; Ma, D.; Green, A. A.; Kelley, S. O.; Pardee, K. A Multiplexed, Electrochemical Interface for Gene-Circuit-Based Sensors. *Nat. Chem.* **2020**, *12* (1), 48−55.

(14) Seo, B.; Choi, S.; Kim, J. Simple Electrochemical Deposition of Au Nanoplates from Au(I) Cyanide Complexes and Their Electrocatalytic Activities. *ACS Appl. Mater. Interfaces* **2011**, *3* (2), 441−446.

(15) Rafatmah, E.; Hemmateenejad, B. Dendrite Gold Nanostructures Electrodeposited on Paper Fibers: Application to Electrochemical Non-Enzymatic Determination of Glucose. *Sensors Actuators, B Chem.* **2020**, *304*, No. 127335.

(16) Xia, Y.; Liu, J.; Huang, W.; Li, Z. Electrochemical Fabrication of Clean Dendritic Au Supported Pt Clusters for Electrocatalytic Oxidation of Formic Acid. *Electrochim. Acta* **2012**, *70*, 304−312.

(17) Khoshfetrat, S. M.; Mehrgardi, M. A. Amplified Electrochemical Genotyping of Single-Nucleotide Polymorphisms Using a Graphene-Gold Nanoparticles Modified Glassy Carbon Platform. *RSC Adv.* **2015**, *5* (37), 29285−29293.

(18) German, N.; Ramanavicius, A.; Ramanaviciene, A. Electrochemical Deposition of Gold Nanoparticles on Graphite Rod for Glucose Biosensing. *Sensors Actuators, B Chem.* **2014**, *203*, 25−34.

(19) Tian, Y.; Liu, H.; Zhao, G.; Tatsuma, T. Shape-Controlled Electrodeposition of Gold Nanostructures. *J. Phys. Chem. B* **2006**, *110* (46), 23478−23481.

(20) Zare, I.; Yaraki, M. T.; Speranza, G.; Najafabadi, A. H.; Shourangiz-Haghighi, A.; Nik, A. B.; Manshian, B. B.; Saraiva, C.; Soenen, S. J.; Kogan, M. J.; Lee, J. W.; Apollo, N. V.; Bernardino, L.; Araya, E.; Mayer, D.; Mao, G.; Hamblin, M. R. Gold Nanostructures:

Synthesis, Properties, and Neurological Applications. *Chem. Soc. Rev.* **2022**, *51* (7), 2601−2680.
(21) Webb, J. A.; Bardhan, R. Emerging Advances in Nanomedicine with Engineered Gold Nanostructures. *Nanoscale* **2014**, *6* (5), 2502−2530.
(22) Malode, S. J.; Ali Alshehri, M.; Shetti, N. P. Nanomaterial-Based Electrochemical Sensors for the Detection of Pharmaceutical Drugs. *Chemosensors* **2024**, *12*, 234.
(23) Zhang, Y.; Chu, W.; Foroushani, A. D.; Wang, H.; Li, D.; Liu, J.; Barrow, C. J.; Wang, X.; Yang, W. New Gold Nanostructures for Sensor Applications: A Review. *Materials (Basel).* **2014**, *7* (7), 5169−5201.
(24) Ritz, A. J.; Stuehr, O. M.; Comer, D. N.; Lazenby, R. A. Controlling Gold Morphology Using Electrodeposition for the Preparation of Electrochemical Aptamer-Based Sensors. *ACS Appl. Bio Mater.* **2024**, *7* (3), 1925−1935.
(25) Mohd Zaki, M. H.; Mohd, Y.; Chin, L. Y. Surface Properties of Nanostructured Gold Coatings Electrodeposited at Different Potentials. *Int. J. Electrochem. Sci.* **2020**, *15* (11), 11401−11415.
(26) Kumar, A.; Gonçalves, J. M.; Sukeri, A.; Araki, K.; Bertotti, M. Correlating Surface Growth of Nanoporous Gold with Electrodeposition Parameters to Optimize Amperometric Sensing of Nitrite. *Sensors Actuators, B Chem.* **2018**, *263*, 237−247.
(27) Zhao, L.; Wang, Y.; Jin, S.; An, N.; Yan, M.; Zhang, X.; Hong, Z.; Yang, S. Rational Electrochemical Design of Hierarchical Microarchitectures for SERS Sensing Applications. *Nat. Synth.* **2024**, *3*, 867−877.
(28) Omidfar, K.; Ahmadi, A.; Syedmoradi, L.; Khoshfetrat, S. M.; Larijani, B. Point-of-Care Biosensors in Medicine: A Brief Overview of Our Achievements in This Field Based on the Conducted Research in EMRI (Endocrinology and Metabolism Research Institute of Tehran University of Medical Sciences) over the Past Fourteen Years. *J. Diabetes Metab. Disord.* **2020**, *23*, 1455.
(29) Khoshfetrat, S. M.; Dorraji, P. S.; Fotouhi, L.; Hosseini, M.; Khatami, F.; Moazami, H. R.; Omidfar, K. Enhanced Electrochemiluminescence Biosensing of Gene-Specific Methylation in Thyroid Cancer Patients' Plasma Based Integrated Graphitic Carbon Nitride-Encapsulated Metal-Organic Framework Nanozyme Optimized by Central Composite Design. *Sensors Actuators B Chem.* **2022**, *364*, No. 131895.
(30) Khoshfetrat, S. M.; Seyed Dorraji, P.; Shayan, M.; Khatami, F.; Omidfar, K. Smartphone-Based Electrochemiluminescence for Visual Simultaneous Detection of RASSF1A and SLC5A8 Tumor Suppressor Gene Methylation in Thyroid Cancer Patient Plasma. *Anal. Chem.* **2022**, *94* (22), 8005−8013.
(31) Wu, C.; Offenhäusser, A.; Mayer, D. A Highly Sensitive Amperometric Aptamer Biosensor for Adenosine Triphosphate Detection on a 64 Channel Gold Multielectrode Array. *Phys. Status Solidi Appl. Mater. Sci.* **2020**, *217* (13), 1−8.
(32) Zhu, Y.; Yao, X.; Yan, K.; Chen, Y.; Zhang, J. A Ratiometric Self-Powered Aptasensor for Simultaneous Detection of Cortisol and Progesterone Based on Spatially Resolved Tri-Channel Photofuel Cell. *Biosens. Bioelectron.* **2023**, *223*, No. 115020.
(33) Contreras Jiménez, G.; Eissa, S.; Ng, A.; Alhadrami, H.; Zourob, M.; Siaj, M. Aptamer-Based Label-Free Impedimetric Biosensor for Detection of Progesterone. *Anal. Chem.* **2015**, *87* (2), 1075−1082.
(34) Sabaté del Río, J.; Woo, H. K.; Park, J.; Ha, H. K.; Kim, J. R.; Cho, Y. K. SEEDING to Enable Sensitive Electrochemical Detection of Biomarkers in Undiluted Biological Samples. *Adv. Mater.* **2022**, *34*, No. 2200981.
(35) Baradoke, A.; Jose, B.; Pauliukaite, R.; Forster, R. J. Properties of Anti-CA125 Antibody Layers on Screen-Printed Carbon Electrodes Modified by Gold and Platinum Nanostructures. *Electrochim. Acta* **2019**, *306*, 299−306.
(36) Shu, H.; Cao, L.; Chang, G.; He, H.; Zhang, Y.; He, Y. Direct Electrodeposition of Gold Nanostructures onto Glassy Carbon Electrodes for Non-Enzymatic Detection of Glucose. *Electrochim. Acta* **2014**, *132*, 524−532.
(37) Pedersen, T.; Fojan, P.; Pedersen, A. K. N.; Magnusson, N. E.; Gurevich, L. Amperometric Biosensor for Quantitative Measurement Using Sandwich Immunoassays. *Biosensors* **2023**, *13*, 519.
(38) Korent, A.; Trafela, Š.; Soderžnik, K. Ž.; Samardžija, Z.; Šturm, S.; Rožman, K. Ž. Au-Decorated Electrochemically Synthesised Polyaniline-Based Sensory Platform for Amperometric Detection of Aqueous Ammonia in Biological Fluids. *Electrochim. Acta* **2022**, *430*, No. 141034.
(39) Saeed, M.; Saddique, Z.; Mujahid, A.; Afzal, A. Discerning Biomimetic Nanozyme Electrodes Based on G-C3N4 Nanosheets and Molecularly Imprinted Polythiophene Nanofibers for Detecting Creatinine in Microliter Droplets of Human Saliva. *Biosens. Bioelectron.* **2024**, *247*, No. 115899.
(40) Jing, L.; Shi, Y. E.; Cui, J.; Zhang, X.; Zhan, J. Hydrophobic Gold Nanostructures via Electrochemical Deposition for Sensitive SERS Detection of Persistent Toxic Substances. *RSC Adv.* **2015**, *5* (18), 13443−13450.
(41) González-Martínez, E.; Saem, S.; Beganovic, N. E.; Moran-Mirabal, J. M. Electrochemical Nano-Roughening of Gold Microstructured Electrodes for Enhanced Sensing in Biofluids. *Angew. Chemie - Int. Ed.* **2023**, *62*, No. e202218080.
(42) Shanmugam, M.; Kim, K. Electrodeposited Gold Dendrites at Reduced Graphene Oxide as an Electrocatalyst for Nitrite and Glucose Oxidation. *J. Electroanal. Chem.* **2016**, *776*, 82−92.
(43) Casaletto, M. P.; Longo, A.; Martorana, A.; Prestianni, A.; Venezia, A. M. XPS Study of Supported Gold Catalysts: The Role of Au0 and Au+ Species as Active Sites. *Surf. Interface Anal.* **2006**, *38*, 215−218.
(44) Chang, H. W.; Chen, C. L.; Chen, Y. H.; Chang, Y. M.; Liu, F. J.; Tsai, Y. C. Electrochemical Organophosphorus Pesticide Detection Using Nanostructured Gold-Modified Electrodes. *Sensors* **2022**, *22* (24), 9938.
(45) Aslam, M.; Fu, L.; Su, M.; Vijayamohanan, K.; Dravid, V. P. Novel One-Step Synthesis of Amine-Stabilized Aqueous Colloidal Gold Nanoparticles. *J. Mater. Chem.* **2004**, *14* (12), 1795−1797.
(46) Gao, X.; Du, X.; Liu, D.; Gao, H.; Wang, P.; Yang, J. Core-Shell Gold-Nickel Nanostructures as Highly Selective and Stable Non-enzymatic Glucose Sensor for Fermentation Process. *Sci. Rep.* **2020**, *10* (1), 1−10.
(47) Muhammad, H.; Tahiri, I. A.; Muhammad, M.; Masood, Z.; Versiani, M. A.; Khaliq, O.; Latif, M.; Hanif, M. A Comprehensive Heterogeneous Electron Transfer Rate Constant Evaluation of Dissolved Oxygen in DMSO at Glassy Carbon Electrode Measured by Different Electrochemical Methods. *J. Electroanal. Chem.* **2016**, *775*, 157−162.
(48) Cao, Q.; Shao, Z.; Hensley, D. K.; Lavrik, N. V.; Venton, B. J. Influence of Geometry on Thin Layer and Diffusion Processes at Carbon Electrodes. *Langmuir* **2021**, *37* (8), 2667−2676.
(49) Gopu, G.; Muralidharan, B.; Vedhi, C.; Manisankar, P. Determination of Three Analgesics in Pharmaceutical and Urine Sample on Nano Poly (3, 4-Ethylenedioxythiophene) Modified Electrode. *Ionics (Kiel).* **2012**, *18* (1−2), 231−239.
(50) Rama Kant, P. Theory for Staircase Voltammetry and Linear Scan Voltammetry Onfractal Electrodes: Emergence of Anomalous Randles-Sevčik Behavior. *Electrochim. Acta* **2013**, *111*, 223−233.
(51) Pande, I.; Pascual, L. F.; Kousar, A.; Peltola, E.; Jiang, H.; Laurila, T. Interface Matters - Effects of Catalyst Layer Metallurgy on Macroscale Morphology and Electrochemical Performance of Carbon Nanofiber Electrodes. *Diam. Relat. Mater.* **2023**, *131*, No. 109566.
(52) Kousar, A.; Peltola, E.; Laurila, T. Nanostructured Geometries Strongly Affect Fouling of Carbon Electrodes. *ACS Omega* **2021**, *6* (40), 26391−26403.
(53) Suni, I. I. Impedance Methods for Electrochemical Sensors Using Nanomaterials. *TrAC - Trends Anal. Chem.* **2008**, *27* (7), 604−611.
(54) Cao, Q.; Hensley, D. K.; Lavrik, N. V.; Venton, B. J. Carbon Nanospikes Have Better Electrochemical Properties than Carbon Nanotubes Due to Greater Surface Roughness and Defect Sites. *Carbon N. Y.* **2019**, *155*, 250−257.


https://doi.org/10.1021/acsanm.5c00962
*ACS Appl. Nano Mater.* XXXX, XXX, XXX−XXX

(55) Patel, J.; Radhakrishnan, L.; Zhao, B.; Uppalapati, B.; Daniels, R. C.; Ward, K. R.; Collinson, M. M. Electrochemical Properties of Nanostructured Porous Gold Electrodes in Biofouling Solutions. *Anal. Chem.* **2013**, *85* (23), 11610−11618.
(56) Leppanen, E.; Akhoundian, M.; Sainio, S.; Etula, J.; Pitkanen, O.; Laurila, T. Structure-Property Relationships in Carbon Electrochemistry. *Carbon N. Y.* **2022**, *200*, 375−389.
(57) Peltola, E.; Aarva, A.; Sainio, S.; Heikkinen, J. J.; Wester, N.; Jokinen, V.; Koskinen, J.; Laurila, T. Biofouling Affects the Redox Kinetics of Outer and Inner Sphere Probes on Carbon Surfaces Drastically Differently-Implications to Biosensing. *Phys. Chem. Chem. Phys.* **2020**, *22* (29), 16630−16640.
(58) Collyer, S. D.; Davis, F.; Lucke, A.; Stirling, C. J. M.; Higson, S. P. J. The Electrochemistry of the Ferri/Ferrocyanide Couple at a Calix[4]Resorcinarenetetrathiol-Modified Gold Electrode as a Study of Novel Electrode Modifying Coatings for Use within Electro-Analytical Sensors. *J. Electroanal. Chem.* **2003**, *549*, 119−127.
(59) Pellitero, M. A.; Curtis, S. D.; Arroyo-Currás, N. Interrogation of Electrochemical Aptamer-Based Sensors via Peak-to-Peak Separation in Cyclic Voltammetry Improves the Temporal Stability and Batch-to-Batch Variability in Biological Fluids. *ACS Sensors* **2021**, *6* (3), 1199−1207.
(60) Rodriguez, M. C.; Kawde, A. N.; Wang, J. Aptamer Biosensor for Label-Free Impedance Spectroscopy Detection of Proteins Based on Recognition-Induced Switching of the Surface Charge. *Chem. Commun.* **2005**, 4267−4269.
(61) Mehrgardi, S. M.; Khoshfetrat, M. A. Electrochemical Genotyping of Single-Nucleotide Polymorphisms by Using Monobase-Conjugated Modified Nanoparticles. *ChemElectroChem* **2014**, *1*, 779−786.
(62) Momeni, F.; Khoshfetrat, S. M.; Zarei, K. Electrochemical Sandwich-Type Aptasensor Based on the Multifunctional Catechol-Loaded Au/MIL-53(Fe) for Detection of Cardiac Troponin I. *ACS Appl. Nano Mater.* **2023**, *6* (20), 19239−19248.


https://doi.org/10.1021/acsanm.5c00962
*ACS Appl. Nano Mater.* XXXX, XXX, XXX−XXX